Superflat energy band induced by moiré electric potential in twisted bilayer graphene

Jie Cao,[1,*] Fenghua Qi,[2,*] Hai Yang,[3] and Guojun Jin[3,4,†]

[1]*College of Science, Hohai University, Nanjing 210098, China*

[2]*School of Electronic Engineering, Nanjing Xiaozhuang University, Nanjing 211171, China*

[3]*School of Physical Science and Technology, Kunming University, Kunming 650214, China*

[4]*National Laboratory of Solid State Microstructures, Department of Physics, and Collaborative Innovation Center of Advanced Microstructures, Nanjing University, Nanjing 210093, China*

(Received 22 October 2020; accepted 13 April 2021; published 23 April 2021)

Narrow and even flat energy bands reflect strong electronic correlation which brings in novel physical properties. Pursuing flatter band has recently attracted a lot of attention. Along this line, we theoretically investigate low-energy band structures and concomitant topological properties of twisted bilayer graphene at the first magic angle based on a continuum model. By considering an external moiré electric potential, in addition to the intrinsic Hartree potential, we find that the lowest bands can be further flattened by this electric potential and a superflat band structure is obtained. In such bands, the extremely small ratio between the bandwidth and the interaction strength will enhance the strong correlation. These superflat energy bands give nearly perfect nesting at the half-filling, then it benefits the formation of Cooper pairs and the rise of superconducting temperature. Moreover, combining with a perfectly aligned boron nitride substrate, the system undergoes a topological phase transition by modulating the relevant parameters of the electric potential. The topological phase transition can be well explained using simplified analytical treatments near the Dirac points.

DOI: 10.1103/PhysRevB.103.165417

I. INTRODUCTION

A recent experimental breakthrough was the fabrication of twisted bilayer graphene with accurately controlled twist angles, and then superconductivity and strongly correlated Mott insulating state were discovered in such a system [1–4]. A twisted graphene bilayer (TGB) is constructed with two rotationally stacked graphene single layers, and its electronic band structure is sensitively dependent on the twist angle θ. At each of a series of magic angles, two nearly flat bands around the neutrality point are formed due to strong interlayer coupling [5–17]. When the carrier density is assured for that the Fermi level lies within the flat bands, the Coulomb interaction, which is much larger than the kinetic energy of an electron, drives the system into a strongly correlated phase. Together with the nontrivial topology of the flat bands, the TGB shows many interesting phenomena. A surge of theoretical works have been done on this subject for explaining and exploring its exotic properties [18–38].

As θ approaches the first magic angle, the noninteracting bandwidth of the lowest bands shrinks to the smallest value about 7 meV. An important issue to be concerned with is if we can compress further the flat bands of a TGB into an extremely narrow one. This is interesting but not very intuitive since previous attempts with external fields, for instance, hydrostatic pressure [3,39] or optical illumination [40], only changes the value of the magic angle rather than the bandwidth. Other studies that try to flatten the low-energy bands of some different moiré structures by introducing gaps at the primary Dirac points [41,42] do not exceed the bandwidth limit of the TGB. If the bandwidth of the flat bands at the magic angle can change with external conditions, it will make the TGB a versatile platform to investigate the strong correlation effects. On the other hand, the effect of the long-range Coulomb interaction on the lowest bands is nonnegligible. The occupation of the lowest bands leads to an inhomogeneous electrostatic potential which is comparable or larger than the bandwidth of the flat bands. Using the Hartree approximation, the effective potential gives rise to a significant distortion of the flat bands [43–48].

In this paper, we consider an external moiré electrostatic potential (MEP) applied on the system in addition to the intrinsic Hartree potential (HP). We investigate the band dispersion and the Chern number of the TGB by using a continuum model in the vicinity of the Dirac points in graphene monolayers (GMLs) [5,10]. It is found that both the external MEP and the intrinsic HP shift the Dirac cones in energy and open gaps at the hexagon corners of the moiré Brillouin zone (MBZ). During the same time, the energy at the Γ point is rarely affected by the intrinsic HP but linearly responds to the external MEP. Hence, the flat conduction (or valence) band is compressed while the other band is stretched when there exists only one potential. This band flattening mechanism does not change the total bandwidth of the flat bands. However, combination of the external MEP and the intrinsic HP can give rise to superflat bands with the total bandwidth less than 2 meV. When the Fermi energy is tuned inside the superflat bands, the velocity of the electron is seriously suppressed in

*These authors contributed equally to this work.

†Corresponding author: gjin@nju.edu.cn

the whole MBZ. This is unlike the noninteracting TGB at the first magic angle, where the velocity is relatively large near the Γ point. The ratio between the bandwidth and the Coulomb interaction is further decreased, then the system is driven into the stronger correlation limit. Together with the nearly perfect nesting at half-filling of the superflat bands, more interesting phenomena can be explored in this platform. We can derive an effective Hamiltonian in the vicinity of the Dirac points. This Hamiltonian can well explain the energy shift and the gap opening simultaneously. Furthermore, it is justified that if we apply the external MEP on the TGB, a topologically trivial gap is opened between the conduction and valence bands. However, an atom-scale staggered sublattice potential generated from a substrate can introduce topologically nontrivial gaps at the Dirac points. Using the benefit of these two competing effects, the system can undergo a topological phase transition via the modulation of an external MEP.

The paper is organized as follows. In Sec. II, we briefly review the effective continuum model for a TGB, and also introduce a MEP. In Sec. III, we calculate the low-energy spectra numerically, and find that the MEP can notably change the band structure and the topology of the TGB. We also show that the effective Hamiltonians in the vicinity of the Dirac points can be used to explain the topological phase transition of the flat bands. In Sec. IV, we discuss the possible experimental realization for compressing the TGB's bands. Finally, we give a brief conclusion in Sec. V.

II. MODEL HAMILTONIAN IN THE CONTINUUM LIMIT

At a small twist angle θ, a slight difference in the lattice orientation gives rise to a long-period moiré interference pattern, which means the number of carbon atoms in a unit cell will be very large. It is a challenging problem to strictly solve the single electron's wave equation in such a complex system. An optional way is to calculate the band structure using a continuum model in the vicinity of the Dirac points in GMLs [5,10,49].

We construct a TGB by rotating layer 1 and layer 2 with angles $-\theta/2$ and $+\theta/2$, respectively, in a totally overlapping graphene bilayer. The moiré unit cell is spanned by L_1 and L_2 as illustrated in Fig. 1(a). The lattice constant $|L_1| = |L_2| = L$ is $L = a/2\sin(\theta/2)$. The lattice structure locally resembles the regular stacking such as AA, AB, or BA. In momentum space, the two Dirac points of the rotated graphene layers are separated by $k_\theta = 2K_0\sin(\theta/2)$, where $K_0 = 4\pi/3a$ and a is the lattice constant of each GML. After the band reconstruction, $+\mathrm{K}_1$ and $-\mathrm{K}_2$ are folded onto one corner ($\overline{\mathrm{K}}'$) of the MBZ of the TGB, while $-\mathrm{K}_1$ and $+\mathrm{K}_2$ are folded onto the other inequivalent corner ($\overline{\mathrm{K}}$), as shown in Figs. 1(b) and 1(c).

When the twist angle is small, the electronic structure can be described by a continuum model, where the intervalley mixing can be safely neglected. In a single valley, taking $\xi = +$ as an example, the low-energy band structure can be described by the Dirac model around the Dirac points of a monolayer shown in Fig. 1(c). We can write the Hamiltonian with the interlayer coupling by the moiré potential $U(\boldsymbol{r})$,

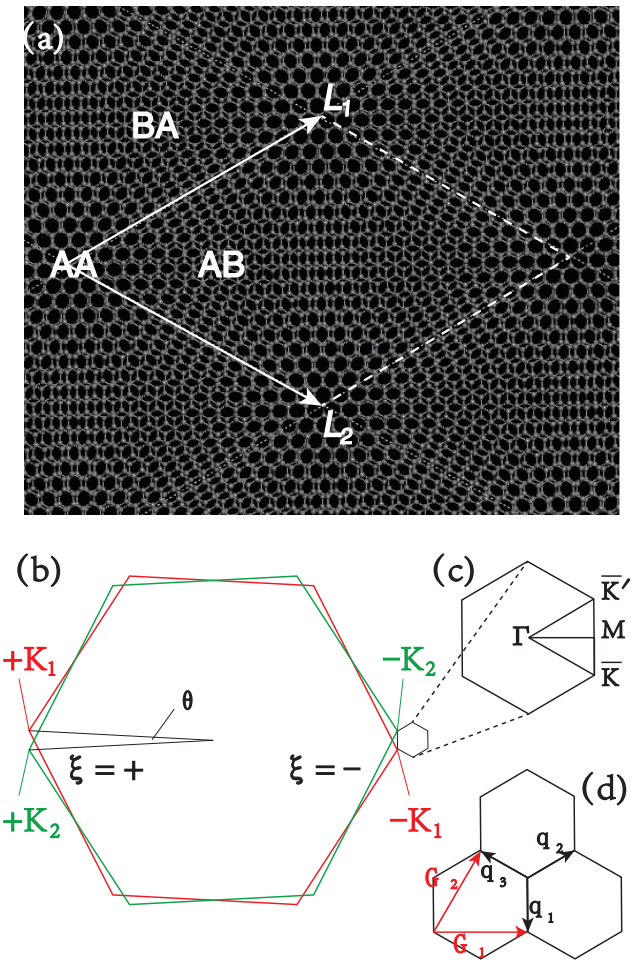

FIG. 1. (a) Atomic structure of a TGB with $\theta = 3.48^\circ$. (b) Brillouin zone folding in the TGB with a small twist angle θ. The two large hexagons represent the first Brillouin zones (BZs) of the two GMLs distinguished by red (layer 1) and green (layer 2), with $\pm\mathrm{K}_{1,2}$ as the valleys in the BZs. (c) The small hexagon is the moiré Brillouin zone (MBZ) of the TGB, with $\overline{\mathrm{K}}$ and $\overline{\mathrm{K}}'$ as the valleys in the MBZ. (d) The three $\boldsymbol{q}_n$ are the momentum transfers that correspond to the three interlayer hopping processes. $\boldsymbol{G}_i$ ($i = 1, 2, 3$) are the reciprocal lattice vectors.

that is

$$\mathcal{H}_0 = \begin{pmatrix} -iv_\mathrm{F}\boldsymbol{\sigma}_{\theta/2}\cdot\boldsymbol{\nabla} & U(\boldsymbol{r}) \\ U^\dagger(\boldsymbol{r}) & -iv_\mathrm{F}\boldsymbol{\sigma}_{-\theta/2}\cdot\boldsymbol{\nabla} \end{pmatrix}, \tag{1}$$

where $\boldsymbol{\sigma}_{\theta/2} = e^{-(i\theta/4)\sigma_z}(\sigma_x, \sigma_y)e^{(i\theta/4)\sigma_z}$, $\boldsymbol{\nabla} = (\partial_x, \partial_y)$, and $U(\boldsymbol{r}) = \sum_{j=1}^{3} U_j e^{-i\boldsymbol{q}_j\cdot\boldsymbol{r}}$. The three-momentum transfers $\boldsymbol{q}_j$ are $\boldsymbol{q}_1 = k_\theta(0, -1)$, $\boldsymbol{q}_2 = k_\theta(\sqrt{3}/2, 1/2)$, and $\boldsymbol{q}_3 = k_\theta(-\sqrt{3}/2, 1/2)$, as shown in Fig. 1(d). The symmetry of the TGB requires the interlayer coupling to have the form

$$U_j = w_{\mathrm{AA}}\sigma_0 + w_{\mathrm{AB}}[\sigma_x\cos(j-1)\phi + \sigma_y\sin(j-1)\phi], \tag{2}$$

where $\phi = 2\pi/3$, and w_{AA} and w_{AB} are the interlayer hopping parameters in the AA and AB stacking regions. In the rest of this paper, we will focus on this valley if there is no special statement.

As our main consideration, we apply an onsite MEP

$$V(\boldsymbol{r}) = \sum_n V_n(\boldsymbol{r}) = \sum_n V_n \sum_{i=1,2,3} \cos(n\boldsymbol{G}_i \cdot \boldsymbol{r}) \qquad (3)$$

on both layers, where $\boldsymbol{G}_1 = k_\theta(\sqrt{3}, 0)$, $\boldsymbol{G}_2 = k_\theta(\sqrt{3}/2, 3/2)$, and $\boldsymbol{G}_3 = \boldsymbol{G}_1 - \boldsymbol{G}_2$ are the reciprocal lattice vectors of the MBZ, as shown in Fig. 1(d). We assume that the origin of the coordinates locates at one of the AA regions. V_n is the amplitude of the potential. To avoid extra multiperiodicities added into the system, we only take two components, i.e., $n = 1, 2$. The form of $V_1(\boldsymbol{r})$ is very natural in the TGB because it is compatible with the charge density distribution. Performing a self-consistent Hartree calculation of the band structure, the long-range Coulomb interaction provides itself an intrinsic electrostatic HP which has the same form as $V_1(\boldsymbol{r})$ [43–48]. In this sense, we use $V_1(\boldsymbol{r})$ to mimic the mean-filed approximation of the Coulomb interactions. On the other hand, $V_2(\boldsymbol{r})$ is an external MEP that can be realized with the electrostatic gating schemes [50–52]. One can pattern an array of periodic fine metal gates on top of graphene samples by etching dielectric layers with a moiré pattern as shown in Fig. 6. For the latter, we will discuss the experiment setup in details in Sec. IV.

Notice that the moiré potentials $U(\boldsymbol{r})$ and $V(\boldsymbol{r})$ hybridize the TGB's eigenstates at $\boldsymbol{q} = \boldsymbol{k} + n_1\boldsymbol{G}_1 + n_2\boldsymbol{G}_2$, where n_1, n_2 are integers. Therefore, the total Hamiltonian $\mathcal{H} = \mathcal{H}_0 + V(\boldsymbol{r})$ for a single Bloch vector $\boldsymbol{k}$ in the MBZ owns the infinite dimensions. As the low-energy states are expected to be dominated by the GML eigenstates near the original Dirac points, we truncate the Hamiltonian to the finite dimensions and just keep $\boldsymbol{q}$ with $|n_1| \leqslant 6$ and $|n_2| \leqslant 6$ [18]. Then, we numerically diagonalize the Hamiltonian and obtain the eigenenergies and eigenstates.

Here, we take $v_F = \sqrt{3}at/2$, where $t = 2.6$ eV is the hopping energy between the nearest-neighbor atoms on a graphene layer. The moiré potential $U(\boldsymbol{r})$, representing the interlayer coupling, is controlled by the two parameters w_{AA} and w_{AB}, which are slightly different in the real TGB. Earlier studies assumed $w_{AA} = w_{AB}$, which corresponds to a perfectly flat TGB [14–16]. Afterwards, deepened theoretical analysis predicted that the optimized lattice structure of the TGB is actually corrugated in the out-of-plane direction. As a result, the interlayer spacing is the widest in the AA stacking region and the narrowest in the AB/BA stacking region. It makes w_{AA} a little smaller than w_{AB}. As shown in a numerical work [18], the difference between w_{AA} and w_{AB} makes sure that the lowest bands at the magic angle are well separated from other higher bands. As a suitable choice, in the following calculations, we take $w_{AA} = 0.08$ eV and $w_{AB} = 0.1$ eV [53].

III. RESULTS AND DISCUSSION

A. Band flattening caused by the MEP

As shown in the previous researches [43–48], the intrinsic MEP caused by the Coulomb interactions can modulate the flat bands in the TGB and make the bandwidth of the conductance or valence band become extremely small with fine tuning of the filling level. In our work, we first reproduce this result by substituting the HP with $V_1(\boldsymbol{r})$, and find

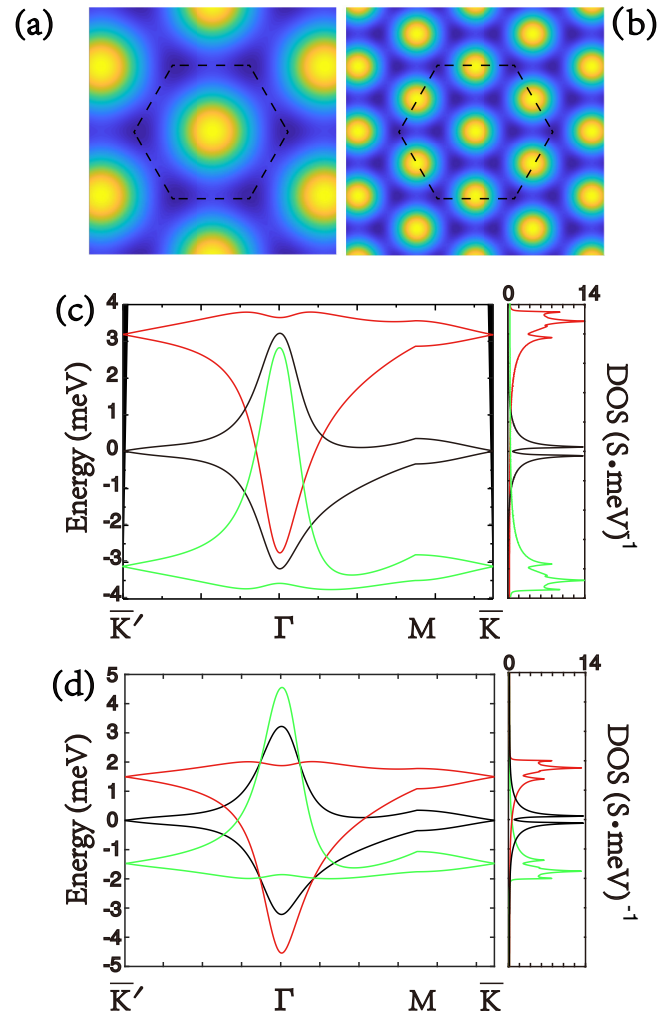

FIG. 2. Schematic of the moiré electric potential (a) $V_1(\boldsymbol{r})$ and (b) $V_2(\boldsymbol{r})$ in real space. The maxima and minima of the potential are denoted by the bright and dark regions, respectively. (c, d) Band flattening of the lowest electronic structures, including the dispersion relations and the densities of states of the TGB without (black) and with the MEP (red and green). The difference is that we set $V_1 = \pm 1.2$ meV, $V_2 = 0$ in (c) and $V_1 = 0$, $V_2 = \pm 3$ meV in (d). $S = (\sqrt{3}/2)L^2$ is the area of a moiré unit.

that the band flattening effect can only be achieved within a small window of the value V_1. In most cases, the band structure is overstretched. If we only consider the presence of $V_1(\boldsymbol{r})$, the electric potential reaches maximum at the AA regions and minimum at the AB/BA regions as illustrated in Fig. 2(a). Since the electric potential preserves the in-plane twofold rotation (C_2) and the time-reversal (T) symmetries, the Dirac points at the MBZ boundaries remain gapless. In Fig. 2(c), we calculate the dispersion relations as well as the densities of states (DOS) at the first magic angle ($\theta = 1.05°$) without and with the MEP. In the absence of the MEP, we can see that the conductance band, as well as the valence band, is about 3 meV wide in the energy axis and separated from the excited bands by an energy gap about 16 meV in the upper and lower sides. When the electric potential $V_1(\boldsymbol{r})$ is applied, the Dirac points are shifted upward (downward)

while the energies at the Γ point are rarely changed. Hence, the conduction (valence) band is compressed by this action. In Fig. 2(c), we set $V_1 = +(-)1.2$ meV and the bandwidth of the conductance (valence) band becomes smaller than 1 meV. In contrast, the bandwidth of the valence (conduction) band, however, is widened twice as much. Due to the fact that the energies at the Γ point are rarely influenced by V_1 and the energies at the Dirac points shift linearly proportional to the value of V_1, both the conduction and the valence band become overstretched if V_1 is further increased.

We can understand this phenomena from the analytical treatment around the corners of the MBZ. In general, we further introduce a C_2T breaking phase parameter φ and let $V_1(\boldsymbol{r})$ has the form $V_1(\boldsymbol{r}) = V_1 \sum_{i=1,2,3} \cos(\boldsymbol{G}_i \cdot \boldsymbol{r} + \varphi)$. As the low-energy states are expected to be dominated by the individual graphene eigenstates near the original Dirac points, the dimension of Hamiltonian (1) can be cutoff to a finite value. By examining the simplest limit in which the momentum lattice is truncated at the first honeycomb shell, the Hamiltonian in the vicinity of the $\overline{\mathrm{K}}$ point is expressed as

$$\mathcal{H}_{\boldsymbol{k}}^0 = \begin{pmatrix} h_{\boldsymbol{k}} & U_1 & U_2 & U_3 \\ U_1^\dagger & h_{\boldsymbol{k}+\boldsymbol{q}_1} & 0 & 0 \\ U_2^\dagger & 0 & h_{\boldsymbol{k}+\boldsymbol{q}_2} & 0 \\ U_3^\dagger & 0 & 0 & h_{\boldsymbol{k}+\boldsymbol{q}_3} \end{pmatrix}, \tag{4}$$

where $\boldsymbol{k}$ is in the MBZ, $h_{\boldsymbol{k}}$ and $h_{\boldsymbol{k}+\boldsymbol{q}_j}$ are the Dirac Hamiltonians of the GML. The dependence of $h_{\boldsymbol{k}}$ and $h_{\boldsymbol{k}+\boldsymbol{q}_j}$ on the twist angle θ is small and can be neglected. Hamiltonian (4) acts on an eight-component spinor wave function $\Psi = (\psi_0, \psi_1, \psi_2, \psi_3)^{\mathrm{T}}$, where ψ_0 comes from layer 2 and ψ_1, ψ_2, ψ_3 come from layer 1.

By solving the Schrödinger equation $\mathcal{H}_{\boldsymbol{k}}\Psi = E_{\boldsymbol{k}}\Psi$, the wave function of the lowest bands satisfies

$$\left(E_{\boldsymbol{k}}^0 - \frac{1-3\alpha^2}{1+6\alpha^2} h_{\boldsymbol{k}}\right)\psi_0 = 0, \tag{5}$$

and

$$\psi_i = -(h_{\boldsymbol{k}+\boldsymbol{q}_i} - E_{\boldsymbol{k}}^0)^{-1} U_i^\dagger \psi_0, \quad (i = 1, 2, 3), \tag{6}$$

where $\alpha \equiv w_{\mathrm{AB}}/v_{\mathrm{F}}k_\theta$. $\mathcal{H}_{\boldsymbol{k}}^0$ and E^0 represent the case without the MEP. This result is first obtained by Bistritzer and MacDonald [10]. At the $\overline{\mathrm{K}}$ point, due to the protection of the C_2T symmetry, $E_0^0 = 0$ for $\boldsymbol{k} = 0$. In this case, ψ_i can be further simplified as $\psi_i = -h_{\boldsymbol{q}_i}^{-1} U_i^\dagger \psi_0$.

In the numerical calculations, it is reasonable to assume $V_1 \ll w_{\mathrm{AB}}$, hence we can treat the electric potential $V_1(\boldsymbol{r})$ as a perturbation term and get the correction of the Hamiltonian using degenerate perturbation theory at the Dirac point as

$$\mathcal{H}_1^{\gamma\beta} = \langle \Psi^\gamma | V(\boldsymbol{r}) | \Psi^\beta \rangle, \tag{7}$$

where γ and β are the conduction and valence band indices of the lowest flat bands, respectively. Because the MEP hybridizes the eigenstates at $\boldsymbol{q} = \boldsymbol{k} + n_1\boldsymbol{G}_1 + n_2\boldsymbol{G}_2$ in the same layer, the Hamiltonian correction at the $\overline{\mathrm{K}}$ point can be rewritten as

$$\begin{aligned} \mathcal{H}_1^{\gamma\beta} &= \textstyle\sum_{i\neq j} \langle \psi_i^\gamma | V_1 e^{i\varphi_{ij}} | \psi_j^\beta \rangle \\ &= \textstyle\sum_{i\neq j} \langle \psi_0^\gamma | U_i h_{\boldsymbol{q}_i}^{-1} V_1 e^{i\varphi_{ij}} h_{\boldsymbol{q}_j}^{-1} U_j^\dagger | \psi_0^\beta \rangle, \end{aligned} \tag{8}$$

where $\varphi_{ij} = \varphi$ if $\boldsymbol{q}_i - \boldsymbol{q}_j = \boldsymbol{G}_{1,2,3}$ and $\varphi_{ij} = -\varphi$ if $\boldsymbol{q}_i - \boldsymbol{q}_j = -\boldsymbol{G}_{1,2,3}$. Transforming Eq. (8) into the same representation as in Eq. (5), we obtain an effective low-energy perturbation Hamiltonian after a little detailed derivation as

$$\mathcal{H}_1^{\mathrm{eff}} = 6V_1\alpha^2 \begin{pmatrix} \cos(\varphi + \pi/3) & 0 \\ 0 & \cos(\varphi - \pi/3) \end{pmatrix}. \tag{9}$$

Notice that V_1 is outside the bracket and $\alpha^2 = 1/3$ at the first magic angle, hence the energy correction is as the same order as V_1. Moreover, two special cases are particularly relevant, i.e., $\varphi = 0$ and $\varphi = \pi$. In these cases, the effective perturbation Hamiltonian is just a unit matrix corresponds to the energy shift of the Dirac points. For $\varphi = 0$ (π), we get the largest positive (negative) energy shift.

It is obvious that the external MEP $V_2(\boldsymbol{r})$ can introduce the similar effects. If we consider only the presence of $V_2(\boldsymbol{r})$, the potential distribution is illustrated in Fig. 2(b). In Fig. 2(d), we can observe similar band flattening effect, and the narrowest bandwidth is less than 0.5 meV if we set $V_2 = \pm 3$ meV. When $V_2(\boldsymbol{r})$ is applied, the energies at the Dirac points are shifted linearly proportional to the value of V_2, while the energies at the Γ point are shifted towards the opposite direction. Due to this tendency, the band structure would also be overstretched if V_2 is relatively large.

It is concluded that with the existence of only $V_1(\boldsymbol{r})$ or $V_2(\boldsymbol{r})$, we cannot obtain a perfect flattened band structure in the TGB. The flattening of the conduction or valence band always accompany with the stretch of the other band. Hence, the total bandwidth, including both the conduction and valence bands, is almost unchanged. Another important issue is that the strength of the long-range Coulomb interactions is much larger than the bandwidth of the noninteracting flat bands at the first magic angle even with large screening effect [44]. Therefore, the band structure is seriously distorted by the effective HP, i.e., $V_1(\boldsymbol{r})$ here, when the filling level is away from the neutrality point. In this sense, it is very necessary to introduce an external MEP into the system to compensate for the serious band distortion caused by the Coulomb interactions. If the external MEP has the form of $V_1(\boldsymbol{r})$, one can restore the noninteracting bands by canceling the influence of the HP in the best scenario. However, if the external MEP has the form of $V_2(\boldsymbol{r})$ due to the fact that $V_2(\boldsymbol{r})$ can effectively manipulate the energy shifts at the Γ point, we can obtain real superflat bands with proper choice of the parameters V_1 and V_2.

B. Superflat bands at the first magic angle

In a wide range of angles close to the first magic angle, the Coulomb interaction strongly exceeds the noninteracting bandwidth of the flat bands. The occupation of the flat bands leads to the effective HP of order $e^2/(\varepsilon L)$, where ε is the dielectric constant of the environment. Even for an unrealistically large screening, the HP can severely distort the band structure of the flat bands [43,44,46]. From the last subsection, we can see that the energy shifts at the Dirac points are almost a factor of 3 larger than the value of V_1. After the modulation of the HP, the bandwidth of the flat bands are equal to or larger than the Coulomb interaction.

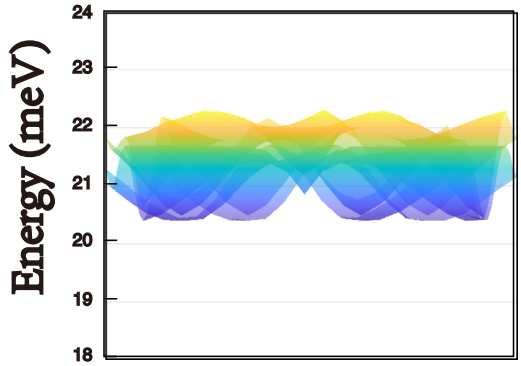

FIG. 3. Superflat bands generated with $V_1 = 15$ meV and $V_2 = -37$ meV. The total bandwidth is less than 2 meV which is a factor of 3 smaller than the total bandwidth of the noninteracting flat bands. The conduction band and the valence band are nearly overlapped with each other.

Fortunately, the effect of the HP can be neutralized by applying an external MEP $V_2(\boldsymbol{r})$. With delicate tuning of V_2, we can even obtain superflat bands at the first magic angle. As shown in Fig. 3, we set $V_1 = 15$ meV and $V_2 = -37$ meV. The resultant flat bands become superflat with total bandwidth less than 2 meV. Figure 3 shows the side view of the flat bands. One can see that the energies of the flat bands are lifted from neutrality all together. Hence, it can be expected that the Wannier wave functions for these bands are not significantly altered, even though in a realistic self-consistent Hartree calculation, the application of $V_2(\boldsymbol{r})$ may influence the charge distribution in the moiré unit cell and then the value of V_1. It should be pointed out that the appearance of the superflat bands is not tied up with some special parameters. In fact, if 10 meV $< V_1 <$ 18 meV, by choosing the right V_2 we always obtain the superflat bands with total bandwidth smaller than 3 meV. This range of V_1 approximately corresponds to the general level-filling cases in TGBs [43].

The appearance of the superflat bands is very sensitive to the twist angle. Due to the nonvanishing Fermi velocity near the Dirac points, superflat bands cannot be generated for the twist angle larger than the first magic one.

C. Nearly perfect nesting at half-filling

Tuning the external MEP can effectively decrease the ratio W/U between the bandwidth W and the Coulomb interaction U, which makes the system a better candidate for research of strong coupling. At the strong coupling, a simple nesting based picture can explain the superconductivity and other instabilities [26–30]. However, when θ gets close to the first magic angle, only small parts of the Fermi surface contribute to the nesting. Therefore, many theoretical works studied the nesting picture a little away from the first magic angle, i.e., $1.2^\circ < \theta < 2^\circ$, even though the ratio W/U is undesirably increased. The reason is quite simple. When θ approaches the first magic angle, the Fermi surface near the van Hove singularity become distorted caused by the competition between the vanishing energy eigenvalues near the corners of the MBZ and the finite energy at the Γ point. In our scheme, we can reduce the Fermi surface deformation near the van Hove singularity

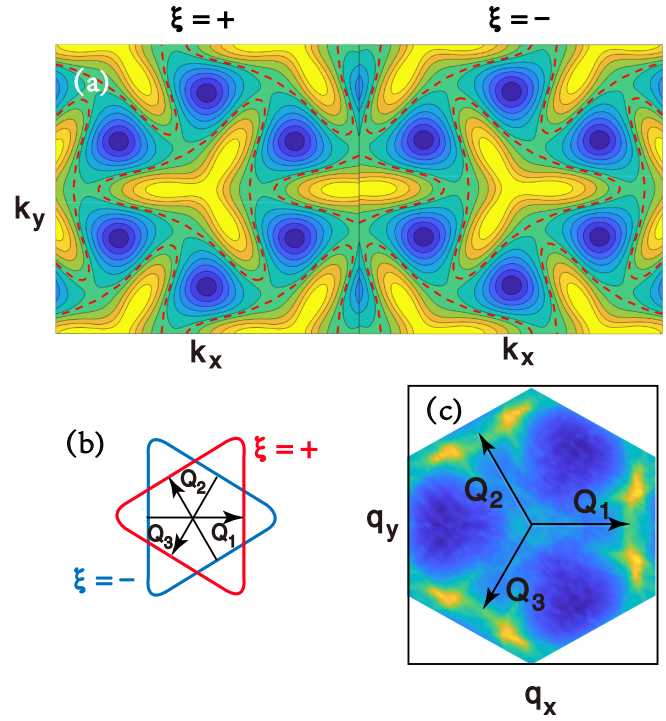

FIG. 4. (a) Contour plots of the compressed conduction bands for $\xi = \pm$ valleys with $V_1 = 12$ meV and $V_2 = -30$ meV. The red dashed loops correspond to the Fermi surface at half filling. With respect to the Fermi surface, the dark regions around the corners of the MBZ are fully filled with electrons while the bright regions at the centers are empty. (b) Perfect nesting of the triangularly shaped Fermi surface. (c) The bare susceptibility in the IVC channel $\chi_0(\boldsymbol{q}) = \langle A_q^\dagger A_q \rangle$. The bright regions near the nesting momenta reach the maximum.

by compressing both the conduction and the valence bands. In Fig. 4(a), we show the contour plots of the conduction band for both valleys $\xi = +$ and $\xi = -$ with $V_1 = 12$ meV and $V_2 = -30$ meV at the first magic angle. The total bandwidth of the flat bands is about 2.2 meV. The value of V_1 corresponds to the half-filling of the conduction bands. The red dashed loops, which resemble perfect triangles, represent the Fermi surface at the half-filling. When the Fermi surface is composed of perfect triangles, like what we plot in Fig. 4(b), then these Fermi pockets are nested along three nesting vectors $Q_{1,2,3}$, as illustrated.

Electronic correlation not only affects the band structure, but also contributes to the transport properties, especially the superconductivity concerned here. To assure the time-reversal symmetry, in the present case, Cooper pairing could come from the strong coupling given in terms of density-dentsity interactions [30] as

$$\mathcal{H}_{\text{int}} = \sum_{\boldsymbol{q}} U n^+_{-\boldsymbol{q}} n^-_{\boldsymbol{q}}, \tag{10}$$

where $n_\xi(\boldsymbol{q}) = \sum_{\boldsymbol{k}} c^{\xi\dagger}_{\boldsymbol{k}+\boldsymbol{q}} c^\xi_{\boldsymbol{k}}$ is the Fourier component of the density operator of the conduction band for valley ξ, and the spin indices are omitted. It is a pure repulsive interaction for which U is taken as positive. Using the random phase approximation (RPA) we can analyze the electron instabilities in all

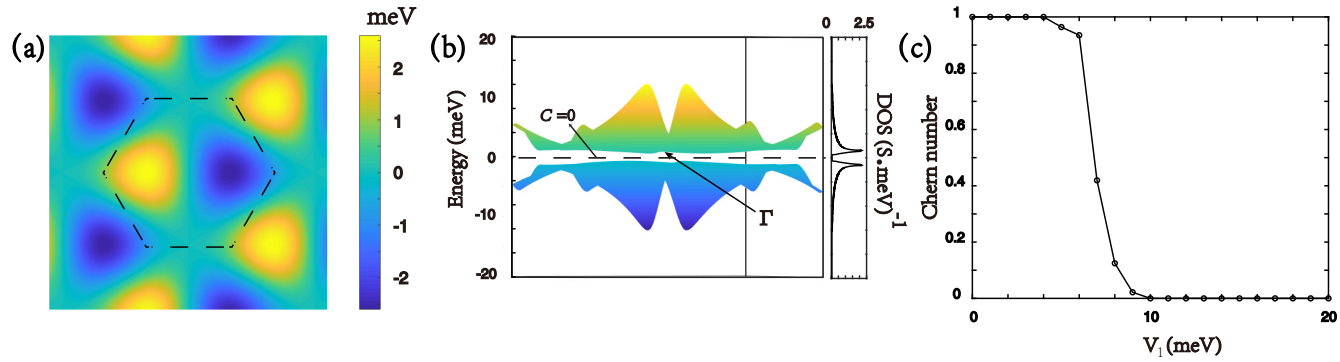

FIG. 5. (a) The moiré electric potential in real space with $V_1 = 1$ meV and $\varphi = \pi/2$. The in-plane C_2 symmetry is broken by the electric potential. (b) Side view of the lowest bands with $V_1 = 20$ meV and $\varphi = \pi/2$. Due to the strong electric potential, the band structure is fully gapped and two energy peaks appear near the Γ point. The Chern number is 0 when the Fermi level lies in this gap. Hence this gap is topologically trivial. (c) Topological phase transition by tuning the electric potential if one of the GMLs in the TGB is nearly aligned with an hBN substrate.

fermion bilinear channels. Although the RPA approach does not include the interwind fluctuations in different channels, it still captures the essential characteristics of the instabilities. From Eq. (10), it is clear that the intervalley coherence (IVC) channel has the strongest instability, and we focus on this channel.

We define an intervalley bilinear operator $A_{\boldsymbol{q}} = \sum_{\boldsymbol{k}} c^{+\dagger}_{\boldsymbol{k}+\boldsymbol{q}} c^{-}_{\boldsymbol{k}}$ and rewrite the interaction Hamiltonian as $\mathcal{H}_{\rm int} \approx -U \sum_{\boldsymbol{q}} A^{\dagger}_{\boldsymbol{q}} A_{\boldsymbol{q}} + \cdots$. By calculating the bare zero frequency susceptibility $\chi_0(\boldsymbol{q}) = \langle A^{\dagger}_{\boldsymbol{q}} A_{\boldsymbol{q}} \rangle$ at low temperatures, the RPA corrected coupling constant in the IVC channel is given by $g_{\rm RPA} = -U/(1 - U\chi_0)$. Figure 4(c) shows the bare susceptibility of the IVC channel that peaks strongly near the three nesting momenta $Q_{1,2,3}$.

The IVC fluctuations can create an effective pairing interaction between electrons [30]. We can see it by recasting the RPA corrected IVC interaction into the intervalley pairing channel, restricting to the zero momentum pairing, i.e., $\sum_{\boldsymbol{q}} g_{\rm RPA}(\boldsymbol{q}) A^{\dagger}_{\boldsymbol{q}} A_{\boldsymbol{q}} \approx -\sum_{\boldsymbol{q},\boldsymbol{k}} g_{\rm RPA}(\boldsymbol{q}) \Delta^{\dagger}_{-\boldsymbol{k}+\boldsymbol{q}} \Delta_{\boldsymbol{k}}$, where $\Delta_{\boldsymbol{k}} = c^{+}_{\boldsymbol{k}} c^{-}_{-\boldsymbol{k}}$ is the intervalley pairing operator. The attractive interaction in the IVC channel implies the repulsive interaction in the intervalley pairing channel. However, the superconducting state can still appear if there is a relative sign change between the pairing form factors connected by the nesting momenta, i.e., $\Delta_{\boldsymbol{k}} = -\Delta_{-\boldsymbol{k}+\boldsymbol{Q}_{1,2,3}}$. When the flat bands are compressed, the RPA corrected coupling diverges faster than the noncompressed case, in addition to the perfect nesting we can expect that the glue effect caused by the IVC fluctuations is stronger in the compression case.

Another critical factor influencing the superconductivity is the DOS at the Fermi energy. From the reports on the TGB [1,3], superconductivities were observed in the vicinity of the van Hove singularity at the first magic angle. Away from the first magic angle $\theta \approx 1.1^{\circ}$, superconductivity is gradually suppressed, and superconductivity is not typically observed with $\theta < 1.0^{\circ}$ or $\theta > 1.2^{\circ}$. These phenomena can be recognized as the decrease of the DOS near the van Hove singularity. On the contrary, when the DOS near the van Hove singularity is strongly increased in the compression case, together with the stronger nesting effect and the diminishing ratio W/U, higher superconducting temperature is expected.

D. Topological phase transition

The effect of the previous MEP does not break the degeneracy at the Dirac points since the MEP preserves the C_2T symmetry. For the simplest case, we ignore $V_2(\boldsymbol{r})$ and focus on the C_2T breaking phase parameter φ to show topological phase transition in the system. If $\varphi \neq 0$ or π, the C_2T symmetry is broken and topological gaps will be generated in the system. It should be noted that similar situation happens for $V_2(\boldsymbol{r})$, however, it is very difficult to obtain analytical results in the more complicated case.

If φ is not set as 0 or π, the electric potential will lose the C_2 symmetry. In Fig. 5(a), we draw the real-space MEP by choosing $\varphi = \pi/2$, and we can see that the maximum and the minimum of the electric potential lie neither in the AA region nor in the AB/BA region. Hence the in-plane C_2 symmetry is no longer preserved. We can rewrite the perturbation Hamiltonian (9) as

$$\mathcal{H}_1^{\rm eff} = f_1(\varphi)\sigma_0 + f_2(\varphi)\sigma_z, \tag{11}$$

where σ_0 is the unit matrix, $f_1(\varphi) = 6V_1\alpha^2 \cos\varphi \cos(\pi/3)$ and $f_2(\varphi) = -6V_1\alpha^2 \sin\varphi \sin(\pi/3)$. The first term in Eq. (11) corresponds to the energy shift of the Dirac cone that is periodic with φ, while the second term is an effective mass term added into the Dirac field. It is worth mentioning that the effective Hamiltonian (11) is only valid at the $\overline{\rm K}$ point, while at the $\overline{\rm K}'$ point the effective Hamiltonian has the same form but by transforming $f_2(\varphi)$ into $-f_2(\varphi)$.

It should be noted that the effective masses at the $\overline{\rm K}$ and $\overline{\rm K}'$ point have opposite signs. To recall that these Dirac cones come from the same valley and have the same chirality, but with opposite mass signs, the total Berry phase of the MBZ is canceled out. With the increase of V_1, the perturbation treatment is no longer valid, however, the Chern number remains unchanged. For $\varphi = \pi/2$ and $\varphi = 3\pi/2$, the Dirac points are pinned down to the zero energy level and the absolute value of the effective mass reaches the maximum. In Fig. 5(b), we show the band structure of the whole MBZ with the amplitude

$V_1 = 20$ meV, and find that a sizable full gap is opened. Using the TKNN formula [54], we numerically checked that the Chern number is 0 when the Fermi level lies within this gap.

On the other hand, if one of the GMLs in the TGB is nearly aligned with an hBN substrate, the broken C_2 symmetry will introduce an atom-scale staggered potential $\Delta \sim 17$ meV in this layer. The effect of top (bottom) layer staggered potential $\Delta_t(\Delta_b)$ on the single-valley moiré Hamiltonian (1) gives effective masses at the $\overline{\mathrm{K}}$ and $\overline{\mathrm{K}}'$ point with same signs [53], hence a topologically nontrivial gap exists in the system by the perfectly aligned hBN substrate. The topology of the flat bands are determined by the competition between these two kinds of potentials, i.e., atom-scale short-range staggered potential versus long-range MEP. In Fig. 5 (c), we set $\Delta_t = 0$ and $\Delta_b = 10$ meV and the Chern number is calculated with the Fermi level at the charge neutrality. With the increase of V_1, topological phase transition is characterized as the Chern number changes from topologically nontrivial $C = 1$ to topologically trivial $C = 0$. This phase transition can be verified by measuring the Hall conductance at three-quarters filling of the conduction (valence) flat band [55,56].

IV. EXPERIMENTAL REALIZATION

Electrostatic superlattices have been known to significantly modify the electronic structure of low-dimensional materials. In the existing experiments, the reported TGB devices are fabricated with two sheets of rotated graphene encapsulated by two hBN sheets using the tear and stack technique [1,2]. Due to the fact that the flat bands lies within the band gap of the hBN, the moiré pattern generated from the hBN and GML lattices results in an external MEP, and the moiré wavelength λ is controlled by the twist angle ϕ between the hBN and GML as

$$\lambda = \frac{1+\nu}{\sqrt{\nu^2 + 2(1+\nu)(1-\cos\phi)}}a, \tag{12}$$

where $\nu \approx 1.81\%$ is the lattice constant mismatch between the hBN and GML. The form of the external MEP $V_2(\boldsymbol{r})$ requires a twist angle $\phi = 1.85^\circ$ at the first magic angle of the TGB. Moreover, the amplitude of the external MEP created by the hBN substrate is compatible with our numerical calculations.

Another flexible approach to obtain useful an MEP can be realized by electrostatic gating schemes [50–52]. Figure 6 shows a schematic of a typical device geometry. An hBN/TGB/hBN sandwich gated by a global top metal gate and a bottom Si gate with a prepatterned SiO_2 substrate in between. A triangular array of holes are etched into the SiO_2 substrate. Applying a bias to the bottom Si gate results in a spatially periodic variation of the displacement field compatible with the etched pattern, which can be used to mimic an MEP. The top gate electrode is used to independently tune the carrier density in the channel.

So far we focused on the setting where the MEP is perfectly aligned with the TGB, i.e., the center of the MEP locates exactly at the rotation center. In more general cases, for experimental realization, it is very difficult to achieve perfect alignment on the atomic scale. If the MEP center does not coincide with the rotation center, we should take into account a displacement vector $\boldsymbol{D}$. Therefore, the MEP is revised as $\boldsymbol{r} \Rightarrow \boldsymbol{r} + \boldsymbol{D}$, and the effective perturbation Hamiltonian (9) will be modified by changing φ to $\varphi + \boldsymbol{G}_i \cdot \boldsymbol{D}$. This does not change the fact that the MEP will shift the Dirac cones in energy axis and create a topologically trivial gap between the conduction and valence bands.

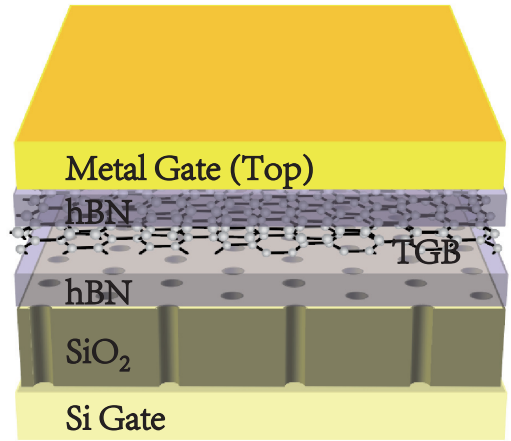

FIG. 6. Schematically showing the device to mimic the MEP. A periodic array of holes are etched into the SiO_2 substrate. Applying a bias to the bottom doped Si gate results in a modulated potential in the TGB.

V. CONCLUSION

In summary, we numerically solved the band structures of a TGB with an external MEP applied onto the system. We found that the MEP has direct influence on the flat bands. Together with the HP caused by the long-range Coulomb interaction, the external MEP can compress the lowest bands in the TGB into a superflat band with the total bandwidth less than 2 meV. The Fermi surface at the half-filling is nearly perfect nested due to the flattening of the bands and higher superconducting temperature is expected. Moreover, combining with a perfect aligned hBN substrate, a topologically trivial or nontrivial gap is opened in the lowest bands. We derived some analytical expressions to understand the mechanism of the topological phase transition. We find that the mass term in the effective Hamiltonian is directly controlled by the MEP. Hence, we can manipulate both the topology and the bandwidth of the flat bands by tuning the MEP. In such a tunable TGB system, systematic investigations of the interplay between the topology and the unconventional superconductivity have deepened our understanding of strong correlation systems.

ACKNOWLEDGMENTS

This work was supported by the Fundamental Research Funds for the Central Universities (Grant No. 2018B58714), Jiangsu Natural Science Foundation (Grant No. BK20190137), the Yunnan Local Colleges Applied Basic Research Projects (Grant No. 2017FH001-001), and the National Natural Science Foundation of China (Grant No. 12074156).

[1] Y. Cao, V. Fatemi, S. Fang, K. Watanabe, T. Taniguchi, E. Kaxiras, and P. Jarillo-Herrero, Nature (London) **556**, 43 (2018).

[2] Y. Cao, V. Fatemi, A. Demir, S. Fang, S. L. Tomarken, J. Y. Luo, J. D. Sanchez-Yamagishi, K. Watanabe, T. Taniguchi, E. Kaxiras, R. C. Ashoori, and P. Jarillo-Herrero, Nature (London) **556**, 80 (2018).

[3] M. Yankowitz, S. Chen, H. Polshyn, Y. Zhang, K. Watanabe, T. Taniguchi, D. Graf, A. F. Young, and C. R. Dean, Science **363**, 1059 (2019).

[4] X. Lu, P. Stepanov, W. Yang, M. Xie, M. A. Aamir, I. Das, C. Urgell, K. Watanabe, T. Taniguchi, G. Zhang, A. Bachtold, A. H. MacDonald, and D. K. Efetov, Nature (London) **574**, 653 (2019).

[5] J. M. B. Lopes dos Santos, N. M. R. Peres, and A. H. Castro Neto, Phys. Rev. Lett. **99**, 256802 (2007).

[6] J. Hass, F. Varchon, J. E. Millán-Otoya, M. Sprinkle, N. Sharma, W. A. de Heer, C. Berger, P. N. First, L. Magaud, and E. H. Conrad, Phys. Rev. Lett. **100**, 125504 (2008).

[7] G. Li, A. Luican, J. M. B. Lopes dos Santos, A. H. Castro Neto, A. Reina, J. Kong, and E. Y. Andrei, Nat. Phys. **6**, 109 (2010).

[8] D. L. Miller, K. D. Kubista, G. M. Rutter, M. Ruan, W. A. de Heer, P. N. First, and J. A. Stroscio, Phys. Rev. B **81**, 125427 (2010).

[9] A. Luican, G. Li, A. Reina, J. Kong, R. R. Nair, K. S. Novoselov, A. K. Geim, and E. Y. Andrei, Phys. Rev. Lett. **106**, 126802 (2011).

[10] R. Bistritzer and A. H. MacDonald, Proc. Natl. Acad. Sci. USA **108**, 12233 (2011).

[11] J. M. B. Lopes dos Santos, N. M. R. Peres, and A. H. Castro Neto, Phys. Rev. B **86**, 155449 (2012).

[12] P. Moon and M. Koshino, Phys. Rev. B **85**, 195458 (2012).

[13] G. Trambly de Laissardière, D. Mayou, and L. Magaud, Phys. Rev. B **86**, 125413 (2012).

[14] P. Moon and M. Koshino, Phys. Rev. B **87**, 205404 (2013).

[15] M. Koshino, New J. Phys. **17**, 015014 (2015).

[16] M. Koshino and P. Moon, J. Phys. Soc. Jpn. **84**, 121001 (2015).

[17] Y. Xu and G. Jin, Europhys. Lett. **111**, 67006 (2015).

[18] M. Koshino, N. F. Q. Yuan, T. Koretsune, M. Ochi, K. Kuroki, and L. Fu, Phys. Rev. X **8**, 031087 (2018).

[19] J. Kang and O. Vafek, Phys. Rev. X **8**, 031088 (2018).

[20] C. Xu and L. Balents, Phys. Rev. Lett. **121**, 087001 (2018).

[21] L. Rademaker and P. Mellado, Phys. Rev. B **98**, 235158 (2018).

[22] J. F. Dodaro, S. A. Kivelson, Y. Schattner, X. Q. Sun, and C. Wang, Phys. Rev. B **98**, 075154 (2018).

[23] F. Wu, T. Lovorn, E. Tutuc, and A. H. MacDonald, Phys. Rev. Lett. **121**, 026402 (2018).

[24] H. C. Po, L. Zou, A. Vishwanath, and T. Senthil, Phys. Rev. X **8**, 031089 (2018).

[25] J. M. Pizarro, M. J. Calderón, and E. Bascones, J. Phys. Commun. **3**, 035024 (2019).

[26] H. Isobe, N. F. Q. Yuan, and L. Fu, Phys. Rev. X **8**, 041041 (2018).

[27] C.-C. Liu, L.-D. Zhang, W.-Q. Chen, and F. Yang, Phys. Rev. Lett. **121**, 217001 (2018).

[28] D. M. Kennes, J. Lischner, and C. Karrasch, Phys. Rev. B **98**, 241407(R) (2018).

[29] H. Guo, X. Zhu, S. Feng, and R. T. Scalettar, Phys. Rev. B **97**, 235453 (2018).

[30] Y.-Z. You and A. Vishwanath, npj Quantum Mater. **4**, 16 (2019).

[31] V. Yu. Irkhin and Yu. N. Skryabin, JETP Lett. **107**, 651 (2018).

[32] Y.-H. Zhang, D. Mao, Y. Cao, P. Jarillo-Herrero, and T. Senthil, Phys. Rev. B **99**, 075127 (2019).

[33] F. Wu and S. Das Sarma, Phys. Rev. Lett. **124**, 046403 (2020).

[34] Y.-H. Zhang, D. Mao, and T. Senthil, Phys. Rev. Research **1**, 033126 (2019).

[35] J. R. Wallbank, M. Mucha-Kruczyński, Xi Chen, and V. I. Fal'co, Ann. Phys. (Berlin) **527**, 359 (2015).

[36] T. M. R. Wolf, O. Zilberberg, I. Levkivskyi, and G. Blatter, Phys. Rev. B **98**, 125408 (2018).

[37] N. R. Finney, M. Yankowitz, L. Muraleetharan, K. Watanabe, T. Taniguchi, C. R. Dean, and J. Hone, Nat. Nanotechnol. **14**, 1029 (2019).

[38] X. Lin and J. Ni, Phys. Rev. B **100**, 195413 (2019).

[39] N. R. Chebrolu, B. L. Chittari, and J. Jung, Phys. Rev. B **99**, 235417 (2019).

[40] O. Katz, G. Refael, and N. H. Lindner, Phys. Rev. B **102**, 155123 (2020).

[41] M. H. Naik and M. Jain, Phys. Rev. Lett. **121**, 266401 (2018).

[42] B. L. Chittari, G. Chen, Y. Zhang, F. Wang, and J. Jung, Phys. Rev. Lett. **122**, 016401 (2019).

[43] F. Guinea and N. R. Walet, Proc. Natl. Acad. Sci. USA **115**, 13174 (2018).

[44] T. Cea, N. R. Walet, and F. Guinea, Phys. Rev. B **100**, 205113 (2019).

[45] L. Rademaker, D. A. Abanin, and P. Mellado, Phys. Rev. B **100**, 205114 (2019).

[46] Z. A. H. Goodwin, V. Vitale, X. Liang, A. A. Mostofi, and J. Lischner, Electron. Struc. **2**, 034001 (2020).

[47] M. J. Calderón and E. Bascones, Phys. Rev. B **102**, 155149 (2020).

[48] M. Xie and A. H. MacDonald, arXiv:2010.07928.

[49] G. Tarnopolsky, A. J. Kruchkov, and A. Vishwanath, Phys. Rev. Lett. **122**, 106405 (2019).

[50] S. Dubey, V. Singh, A. K. Bhat, P. Parikh, S. Grover, R. Sensarma, V. Tripathi, K. Sengupta, and M. M. Deshmukh, Nano Lett. **13**, 3990 (2013).

[51] M. Drienovsky, F.-X. Schrettenbrunner, A. Sandner, D. Weiss, J. Eroms, M.-H. Liu, F. Tkatschenko, and K. Richter, Phys. Rev. B **89**, 115421 (2014).

[52] C. Forsythe, X. Zhou, K. Watanabe, T. Taniguchi, A. Pasupathy, P. Moon, M. Koshino, P. Kim, and C. R. Dean, Nat. Nanotechnol. **13**, 566 (2018).

[53] J. Cao, F. Qi, H. Yang, and G. Jin, Phys. Rev. B **101**, 155419 (2020).

[54] D. J. Thouless, M. Kohmoto, M. P. Nightingale, and M. den Nijs, Phys. Rev. Lett. **49**, 405 (1982).

[55] A. L. Sharpe, E. J. Fox, A. W. Barnard, J. Finney, K. Watanabe, T. Taniguchi, M. A. Kastner, and D. Goldhaber-Gordon, Science **365**, 605 (2019).

[56] M. Serlin, C. L. Tschirhart, H. Polshyn, Y. Zhang, J. Zhu, K. Watanabe, T. Taniguchi, L. Balents, and A. F. Young, Science **367**, 900 (2020).